

# A parallel particle cluster algorithm using nearest neighbour graphs and passive target communication

Matthias Frey\*, Steven Böing†, Rui F. G. Apóstolo‡

## Abstract

We present a parallel cluster algorithm for  $N$ -body simulations which uses a nearest neighbour search algorithm and one-sided messaging passing interface (MPI) communication. The nearest neighbour is defined by the Euclidean distance in three-dimensional space. The resulting directed nearest neighbour graphs that are used to define the clusters are split up in an iterative procedure with MPI remote memory access (RMA) communication. The method has been implemented as part of the elliptical parcel-in-cell (EPIC) method targeting geophysical fluid flows. The parallel scalability of the algorithm is discussed by means of an artificial and a standard fluid dynamics test case. The cluster algorithm shows good weak and strong scalability up to 16,384 cores with a parallel weak scaling efficiency of about 80% for balanced workloads. In poorly balanced problems, MPI synchronisation dominates execution of the cluster algorithm and thus drastically worsens its parallel scalability.

## Keywords

distributed-memory parallelism, cluster algorithm, nearest-neighbour graphs,  $N$ -body simulation, one-sided communication, remote memory access (RMA), passive target communication, message passing interface (MPI)

## 1 Introduction

The identification of nearby or nearest neighbours is fundamental to problems in statistical learning (e.g. classification and regression) and in force calculations of  $N$ -body simulations (e.g. molecular dynamics, smoothed-particle hydrodynamics and particle-in-cell). While the former considers closeness in terms of data similarity, the latter uses the spatial distance between two finite size or point particles as a measure. This paper focuses on the nearest neighbour search (NNS) associated with particle-particle (PP) interactions in  $N$ -body simulations. In our case, we use only the single nearest neighbour.

A well-known application of the more general case with multiple neighbours is the Verlet list (or neighbour list) (Verlet, 1967), used in molecular dynamics to reduce the computational complexity for the evaluation of short-ranged non-bonded interactions, often fitted by a Lennard-Jones potential. For each particle, the method stores all neighbouring particles within a cut-off radius in a list or array data structure and evaluates the resulting force on a particle based solely on the stored neighbours. A similar approach is the cell linked list (or cell lists) method (Quentrec and Brot, 1973). This method divides the domain into isotropic grid cells and evaluates the short-range forces on a particle by iterating through all the particles inside that same cell and its neighbouring cells. Hence, this method creates a list of particles per cell rather than per particle as for the Verlet list. Both cell lists and Verlet list are used for other applications such as fluid dynamics simulated with smoothed particle hydrodynamics (Domínguez et al., 2011). In the calculation of gravitational or electrostatic forces as they appear in cosmology or plasma simulations, respectively, the domain partitioning, as carried out with the fast multipole method (FMM) or the Barnes-Hut algorithm, naturally leads to tree data structures. These tree-based methods enable the efficient evaluation of the short- and long-range force contributions. Here, we only focus on interactions between the nearest neighbours. In

\*Mathematical Institute, University of St Andrews, KY16 9SS, UK

†University of Leeds/Met Office Strategic Research Group, School of Earth and Environment, LS2 9JT, UK

‡EPCC, The University of Edinburgh, EH8 9BT, UK

particle-mesh methods (e.g. particle/parcel-in-cell), on the other hand, the domain is already partitioned into usually isotropic grid cells. All particles within a grid cell can therefore be obtained by simple integer arithmetic. Finding near neighbours via grid cell indices has also been applied in other contexts, in e.g. (Bentley, 1975; Yuval, 1975, 1976; Bentley et al., 1977), where the mesh width spacing corresponded to a search radius.

Here, we report the implementation of a parallel cluster algorithm based on a NNS that is used to merge nearby parcels (finite size particles) as part of the elliptical parcel-in-cell (EPIC) (Frey et al., 2022, 2023) method. The EPIC method is based on the idea of using deformable Lagrangian parcels of elliptical shape in order to better capture the dynamics of turbulent fluid flows. Elongated parcels are split into two in order to maintain the effective subgrid scale resolution of the flow, and to avoid numerical problems that arise from parcels with large aspect ratio. To reduce the computational cost, very small parcels obtained through successive splitting are merged with their closest neighbour. The algorithm involves two stages: the first step constructs the nearest neighbour graphs (NNGs), where only small parcels point to their nearest neighbour, which can either be a small or big parcel. In the second step, the NNGs are split in an iterative procedure to avoid parcel chains that would result in elongated ellipsoids. While we use standard point-to-point communication during the NNG construction step, the split-up-stage is implemented with one-sided (or remote memory access) communication.

The remote memory access (RMA) communication was introduced to the message passing interface (MPI) with the MPI 2.0 standard (Message Passing Interface Forum, 1997). Later, the MPI 3.0 standard (Message Passing Interface Forum, 2012) aimed to improve the RMA interface to help overcome performance issues, see e.g. (Hoeffler et al., 2015). Scalability problems of MPI RMA implementations are also addressed by Jiang et al. (2004); Zhao et al. (2016); Schuchart et al. (2021, and references therein). These issues may be the reason why this relatively new MPI feature has so far only been used in a handful of applications, for example (Sawyer and Mirin, 2007; Yamazaki et al., 2019) and (Ghosh et al., 2019). However, Ghosh et al. (2016) has demonstrated that RMA performs better in graph applications than conventional non-blocking point-to-point communication.

This paper is organised as follows: in Section 3 we first summarise the nearest neighbour clustering algorithm and explain its parallelisation in detail. This is followed by benchmark results in Section 4. Final remarks are provided in Section 5.

## 2 One-sided communication

As introduced with MPI 2.0 (Message Passing Interface Forum, 1997) and then further specified with MPI 3.0 (Message Passing Interface Forum, 2012), one-sided communication denotes a paradigm change from the classical point-to-point communication where both sender and receiver have information about the metadata of the message. One-sided communication is well suited for situations where the receiving process (or target) does not or is not required to know the sending process (or origin). Despite this flexibility, one-sided communication comes with its own challenges, mainly the synchronisation of memory accesses to avoid race conditions. There are two synchronisation methodologies: *active* and *passive* target communication. In passive target communication the origin process locks and unlocks the memory location on the receiving (or target) process, which does not engage in the synchronisation. Active target communication, on the other hand, still involves the receiving process, but only the sender possesses information about the metadata. In both cases a so-called *epoch* denotes the time frame in which remote memory accesses (RMAs) are carried out. An epoch with active target communication starts and ends with a call to `MPI_Win_fence` as shown in Fig. 1a, which is a collective operation. On the other hand, an epoch with passive target communication is encapsulated by the non-collective calls to `MPI_Win_lock` and `MPI_Win_unlock` as specified in Fig. 1b. Here, we make use of passive target communication because not all MPI ranks as part of the communicator may be involved in the algorithm performing RMA operations.

In addition to the classification of synchronisation methods, there are two types of memory models: separate and unified. The separate memory model distinguishes between private and public copy as illustrated with the left drawing in Fig. 2. The private copy refers to the local memory of the owning process. The public copy is a dedicated memory region, referred to as *window* in the MPI standard, in which other processes may read (or get) and write (or put) information. A drawback of this memory distinction is the requirement

<pre> ! Begin RMA epoch: call MPI_Win_fence(...) ! Perform RMA operations: call MPI_Put(...) call MPI_Get(...) ! End RMA epoch: call MPI_Win_fence(...) </pre>	<pre> ! Begin RMA epoch: call MPI_Win_lock(...) ! Perform RMA operations: call MPI_Put(...) call MPI_Get(...) ! End RMA epoch: call MPI_Win_unlock(...) </pre>
(a) Active target communication.	(b) Passive target communication.

Figure 1: Incomplete Fortran sample code to demonstrate RMA operations with either active or passive target communication.

of additional synchronisation calls in case the owning process is also updating its local memory during an epoch. In the unified memory model, on the other hand, all processes access the same memory region enabling real-time updates as depicted with the right drawing in Fig. 2. The parallel algorithm presented in Section 3 makes use of passive target communication and requires the unified memory model.

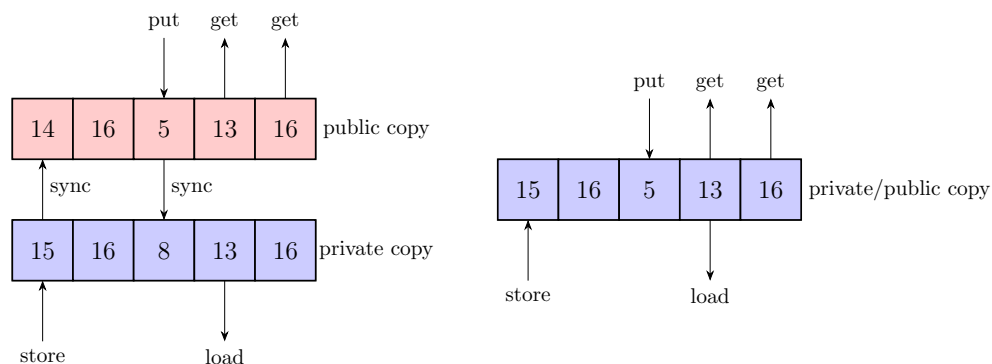


Figure 2: Separate (left) and unified (right) memory model for the remote memory access communication. In the unified model, the public and private copy are identical. The separate memory model requires frequent synchronisation calls to ensure memory coherence. Such calls are denoted by the arrows labelled ‘sync’.

### 3 Nearest neighbour clustering algorithm

The nearest neighbour cluster algorithm described here was developed as part of the EPIC method (Frey et al., 2022, 2023). The algorithm consists of two major steps: the graph construction, and graph resolution. The graph construction step identifies the nearest neighbour based on the Euclidean distance. For this purpose, each object (an ellipsoid in our case) is assigned to its nearest grid point on a Cartesian node-centred mesh. It should be noted that each grid cell contains many parcels, usually of the order of 20. This domain discretisation reduces the operation count of the nearest neighbour search from  $N^2$  to  $8N_{\text{cell}}$ , where  $N$  is the total number of objects and  $N_{\text{cell}}$  represents an average number of objects per grid box in 3D space. For each object, we then search for its nearest neighbour over all the surrounding grid cells and establish a unidirectional link. If two objects point to each other, we call this a dual link. The terminology we use here follows that in previous publications on EPIC. A more extensive discussion of some of the properties of nearest neighbour graphs is also given in Eppstein et al. 1997. This includes generalisation from 1 to  $k$  nearest neighbours. For a set of points that are connected in the graph, there can only be one such dual link, since each parcel only points to one other parcel. Longer cycles are excluded (this could only happen with 3 or more parcels at the exact same distance from each other, which is extremely unlikely). After the search operation is complete, we are left with unweighted directed graphs (DGs). An example of a DG is shown in Fig. 3. A directed graph  $G = (V, E)$ , defined as a set of vertices  $V$  and a set of edges  $E$  obtained

through the aforementioned procedure, has the following properties:

- The **outdegree** of each vertex  $v \in V$  is  $\deg^+(v) \leq 1$ . A parcel which does not need merging has  $\deg^+(v) = 0$ .
- The **indegree** of a vertex  $v \in V$  is  $\deg^-(v) \geq 0$ .

We denote an edge pointing from vertex  $v_1$  to vertex  $v_2$  by  $e_{12} = (v_1, v_2)$ . A vertex  $v \in V$  with **indegree**  $\deg^-(v) = 0$  is called a leaf. In Fig. 3 we colour all leaf vertices, A, B, G, J, K and L, in blue. We denote the collection of leaf vertices by  $\mathbb{L} := \{v \in V \mid \deg^-(v) = 0\}$ . We further define the set of vertices available for merging by  $\mathbb{A} := \mathbb{L} \cup \{v \in V \mid \deg^-(v) > 0 \wedge \forall e_j = (v_j, v) \in E, v_j \in \mathbb{L}\}$ , i.e. all vertices that are either a leaf or have only incoming links from leaf vertices. In terms of the graph in Fig. 3, this condition is satisfied by the vertices F and I as well as the leaf vertices mentioned before. A subgraph  $G_s \subseteq G$  which only consists of vertices that are in  $\mathbb{A}$  can be merged.

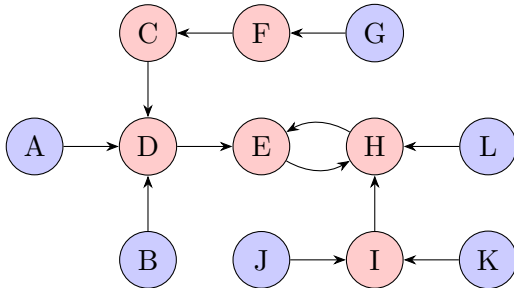


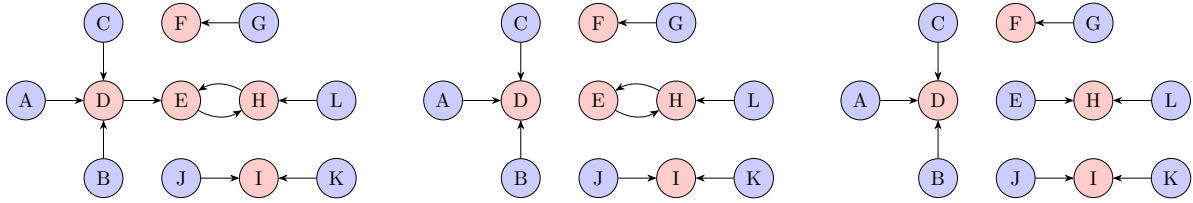
Figure 3: An example of an unweighted directed graph (DG). We call all nodes without an incoming edge *leaf vertices*. This DG has leaf vertices A, B, G, J, K and L.

After the graph construction, the directed graphs are split into subgraphs  $G_s$  in order to avoid large cluster chains. This two-stage process ensures that after both stages all vertices are contained in  $\mathbb{A}$  such that they can be merged. The first stage is an iterative procedure where in each iteration connections between non-leaf nodes are dissolved. However, this stage excludes dual links, i.e. connections between two vertices that point to each other. For the directed graph in Fig. 3, the algorithm performs two iterations as shown in Fig. 4. First, the edges from vertex F to C and I to H are removed (cf. Fig. 4a). The former edge removal results in  $\deg^-(C) = 0$ , i.e. C is a leaf vertex. In the second iteration the edge from D to E is removed (cf. Fig. 4b). After these two iterations, the original cluster is split into four smaller subgraphs. However, the subgraph consisting of vertices E, H and L features a dual link that must be simplified. The algorithm therefore enters the second stage. Here, the edge from H to E is broken up (cf. Fig. 4c) because  $\deg^-(H) > 1$ . For further details on the serial algorithm we refer to (Frey et al., 2022, appendix D).

### 3.1 Details concerning distributed-memory parallelism

The parallel version of the nearest neighbour clustering algorithm presented here was developed with atmospheric simulations in mind, where the vertical dimension is kept serial. However, this only affects the graph construction step, which could be easily extended to a three-dimensional MPI domain decomposition. We further use periodic boundary conditions in both horizontal dimensions, but the method also works, subject to minor modifications, for solid boundary conditions.

In the first step of the algorithm, all objects that are supposed to be clustered with their nearest neighbour are determined. In EPIC, the criterion for ellipsoids to be merged is their volume: if it decreases enough, which can happen due to successive splitting, ellipsoids are merged. A change in the criterion would require only a minor modification. During this search process, the position of objects that need merging and are near domain boundaries are sent to MPI ranks owning adjacent domains, and the receiving MPI ranks append them to their own attribute containers. Objects that are received from other MPI ranks are referred to as *remote objects*, and objects that are located in the subdomain owned by the same MPI rank are referred to



(a) Iteration 1 of stage 1: Remove the edges from F to C and I to H. (b) Iteration 2 of stage 1: Remove the edge from D to E. (c) Stage 2: Remove the edge from H to E.

Figure 4: Graph resolving step for the graph illustrated in Fig. 3. The algorithm consists of two stages. In the first stage, an iterative procedure performs two iterations illustrated in (a) and (b). The second stage eliminates all dual links as shown in (c). After these stages we are left with four smaller subgraphs.

as *local objects*. A sketch illustrating the communication of small objects near domain boundaries from the perspective of MPI rank 0 is given in Fig. 5. Here, small objects marked by ellipses are coloured in blue. Their remote copies are coloured in red. The arrows between the ellipses denote the evaluation of the Euclidean distance to find their nearest neighbour. After this operation is complete, an MPI sub-communicator is constructed which only contains MPI ranks having small objects, i.e. local and/or remote. The aim of this sub-communicator is to reduce the overhead of MPI synchronisation and MPI collective communication during the graph resolution step when the distribution of small objects is spatially concentrated. This subset of MPI ranks then proceeds at locally determining the nearest other object by evaluating the Euclidean distance. For this purpose, these MPI ranks fill four contiguous arrays storing the indices of small objects *isma*, the indices of the locally closest objects *iclo*, the MPI ranks owning the closest object *rclo* and the distances between the small object and its closest object *dclo*. Note that if no close object for remote objects is found locally, the value of *dclo* is set to some big value, here  $L_x^2 + L_y^2 + L_z^2$  where  $L_x$ ,  $L_y$  and  $L_z$  are the domain lengths in the three Cartesian dimensions.

In order to determine the closest neighbour of domain-boundary objects globally, the information of remote objects, i.e. the values of *isma*, *iclo* and *dclo*, is sent back to the original MPI rank owning the small object. The receiving MPI rank then updates the values of *iclo*, *dclo* and *rclo* of the appropriate entry in *isma* if a shorter distance is detected. After this step, the arrays *isma*, *iclo* and *rclo* are properly set and can be used during the iterative procedure of the graph resolution.

During the graph resolution algorithm we use three boolean-typed arrays — i.e. arrays which can store *true/false* values — to keep track of leaf and available vertices as well as vertices that are already part of a final cluster. These three arrays are exposed through MPI windows in order to perform RMA operations, i.e. one-sided communication. The pseudocode of the graph resolution algorithm is provided in Algorithm 1. Steps that involve RMA operations, i.e. `MPI_Get` or `MPI_Put`, are highlighted in orange colour, and steps that denote collective or synchronisation MPI are coloured in cyan. Note that MPI synchronisation calls (e.g. `MPI_Barrier` or `MPI_Win_fence`) are also collective, but we prefer to distinguish between synchronisation and other collective operations such as reductions (e.g. `MPI_Reduce`, `MPI_Allreduce`). In total, the algorithm presented has one `MPI_Allreduce` and five `MPI_Barrier` operations. However these operations can be performed more often due to the iterative procedure (i.e. `while` loop) of the algorithm. Table 1 summarises the number of these kinds of MPI calls for the test cases presented in Section 4. These barrier operations are used for the correctness of the parallel execution because the algorithm performs graph decisions in stages that involve modifications of local and/or remote data via MPI RMA operations. The barriers therefore ensure that all MPI ranks have completed their operations before performing a next step of the algorithm.

The `while` loop from line 3 to line 12 in Algorithm 1 denotes the first stage of the algorithm where all connections of a directed graph are broken up until there are only dual links left. For example, the directed graph of Fig. 3 is broken up into four smaller graphs as shown in Fig. 4a where the graph consisting of vertices E, H and L still has a dual link between E and H. All other graphs that only consist of single links are considered resolved and therefore no longer considered in the process. Since dual links are neither contained in the set of leaf vertices  $\mathbb{L}$  nor in the set of available vertices  $\mathbb{A}$ , the exit condition of the `while`

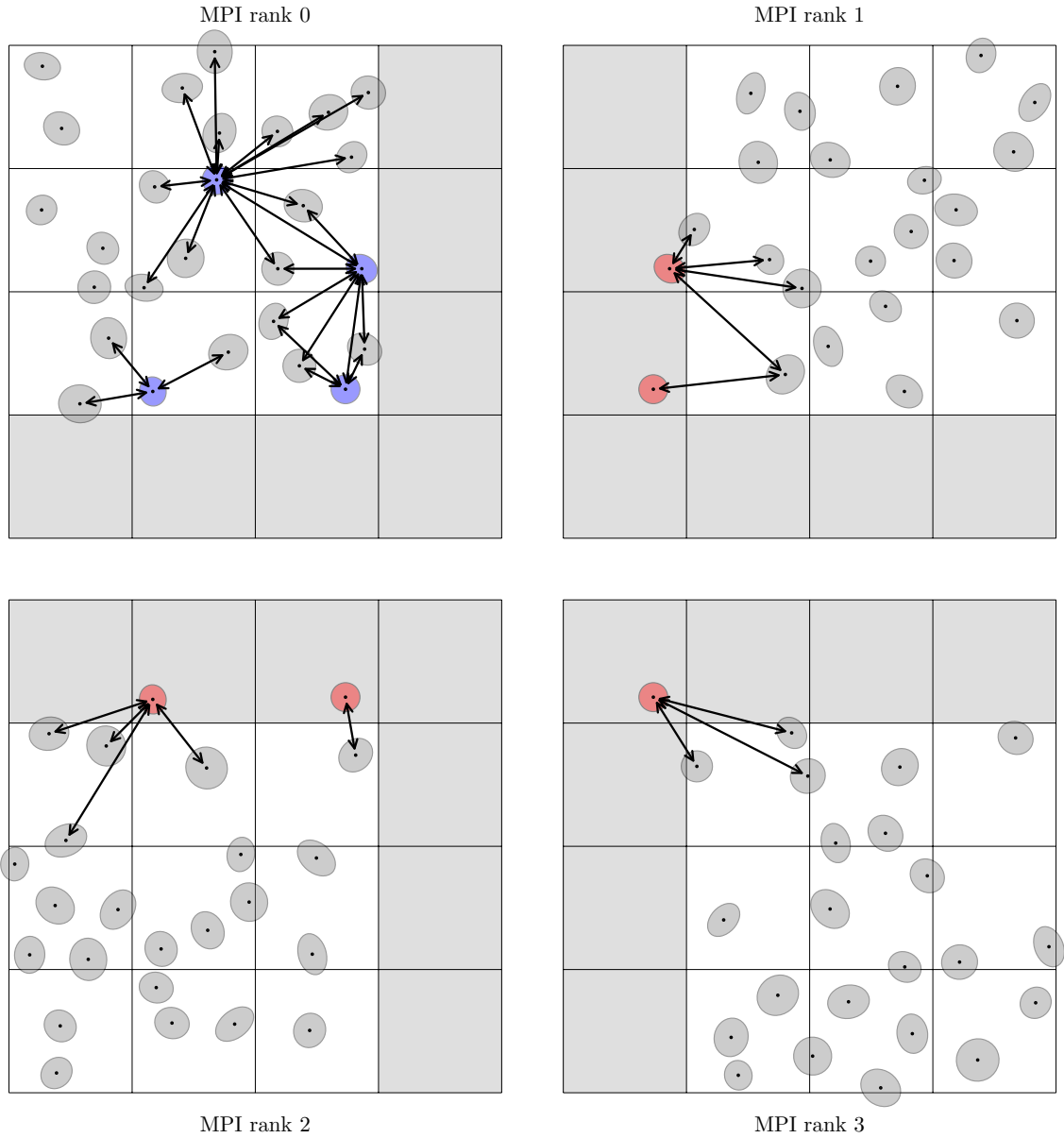


Figure 5: Sketch of finding the nearest neighbour across MPI subdomains. The grey grid cells denote halo (or ghost) cells that overlap with other MPI subdomains. The ellipses highlighted in blue denote small objects in the subdomain owned by MPI rank 0 that are marked for merging. The ellipses in red are duplicates of blue ellipses in boundary regions that are sent to neighbouring MPI ranks (here MPI ranks 1, 2 and 3). The double-headed arrows indicate the evaluation of the Euclidean distance measure between ellipses in the same or adjacent grid cells.

Table 1: Total number of collective and synchronisation MPI calls as well as maximum number of MPI RMA operations across all MPI ranks during the graph resolution for the artificial parcel configuration (cf. Section 4.1) and Rayleigh-Taylor (RT) instability (cf. Section 4.2) example (both examples contain 100 cycles). Note that the number of synchronisation and collective communication calls for the artificial configuration depends on the number of executing MPI ranks because each MPI rank samples its parcels randomly resulting in different configurations.

example	scaling test case	MPI allreduce	MPI barrier	MPI RMA
artificial	strong ( $512^2 \times 32$ )	606 – 619	2,018 – 2,057	304,682 – 4,869,014
	strong ( $1024^2 \times 32$ )	628 – 653	2,084 – 2,159	313,913 – 10,059,186
	strong ( $2028^2 \times 32$ )	678 – 694	2,234 – 2,282	657,091 – 10,511,488
	weak	596 – 725	1,988 – 2,375	2,371,379 – 3,023,677
RT instability	balanced workload	500	1,700	231,284 – 1,770,802
	imbalanced workload	1,080	3,440	4,800,473 – 26,408,101

loop is fulfilled as soon as only dual links remain to be broken up. The dual links are then eliminated in the second stage of the algorithm which corresponds to lines 13–17. Special care must be taken with isolated dual links. These are graphs that only consist of two vertices that point to each other. They are resolved separately because there is no information from its subgraph in order to break up one of the links. For example, the graph in Fig. 4b with the dual link between E and H has the additional connection between H and L. This latter connection uniquely defines the order of elimination, i.e. the link from H to E is deleted. With isolated dual links there is no such decisive logic, which is why each of the two links can be removed. To prevent the removal of both links if the two vertices do not belong to the same MPI rank, the MPI rank with the lower process number eliminates its connection.

---

#### Algorithm 1 Graph resolution

---

- 1: Let  $m \in \{1, \dots, N_{\text{small}}\}$  where  $N_{\text{small}}$  is the number of MPI local small objects.
  - 2: Let  $ic = iclo(m)$  denote the index of a close object.
  - 3: Let  $isma$  be an array of size  $N_{\text{small}}$  that stores the indices of small objects.
  - 4: Let  $rclo$  be an array of size  $N_{\text{small}}$  that stores the MPI ranks owning close objects.
  - 5: **while**  $\mathbb{A} \neq \emptyset \wedge \mathbb{L} \neq \emptyset$  **do**
  - 6: Reset properties for candidate mergers (MPI RMA put on  $l_{\text{available}}(ic)$ )
  - 7: MPI barrier synchronisation
  - 8: Determine leaf parcels (MPI RMA put on  $l_{\text{leaf}}(ic)$ )
  - 9: MPI barrier synchronisation
  - 10: Filter unavailable vertices (MPI RMA put on  $l_{\text{available}}(ic)$ )
  - 11: MPI barrier synchronisation
  - 12: Identify mergers (MPI RMA get on  $l_{\text{available}}(ic)$  and put on  $l_{\text{merged}}(ic)$ ).
  - 13: Collective MPI\_Allreduce reduction
  - 14: **end while**
  - 15: Mark non-leaf parcels as available (MPI RMA put on  $l_{\text{available}}(ic)$ ).
  - 16: MPI barrier synchronisation
  - 17: Resolve dual links (MPI RMA get on  $l_{\text{leaf}}(ic)$  and get on  $l_{\text{available}}(ic)$ )
  - 18: MPI barrier synchronisation
  - 19: Resolve isolated dual links (MPI RMA get on  $l_{\text{available}}(ic)$ )
  - 20: Remove eliminated edges such that the arrays  $isma$ ,  $iclo$  and  $rclo$  are contiguous
-

## 4 Parallel Performance Analysis

In this section we report the merger statistics as well as the parallel performance of the algorithm by means of two examples. The first example demonstrates the parallel scalability using artificial parcel configurations. The second example uses parcel configurations that are obtained from a fully evolved Rayleigh-Taylor instability simulation set up according to (Frey et al., 2023). All benchmarks for this study are performed on ARCHER2, a supercomputer with two AMD EPYC™ 7742 64-core processors per compute node, i.e. 128 cores per compute node. The CPU frequency is tunable to 1.5 GHz, 2 GHz or 2.25 GHz. The latter activates turbo boost which allows a CPU frequency beyond 2.25 GHz. In all results presented here, we use 2 GHz. Each core has a private L1 cache of size 32 KB (i.e.  $32 \cdot 1024$  bytes) and 512 KB of private L2 cache. The L3 cache is shared among 4 cores and consists of 16 MB. The compute nodes are linked with a HPE Slingshot interconnect.

Before assessing the performance of the parallel algorithm, however, we verified its correctness. For this purpose, we compared the results obtained with 16, 32, 64, 128 and 256 cores to the serial version of the algorithm for 1,000 random initial parcel configurations. The test domain spans the cube  $[0, 1]^3$  and is discretised with  $32^3$  isotropic grid cells. A parcel configuration is generated by randomly sampling 40 parcels per grid cell where each parcel is assigned random parcel properties according to Table 2. Their volumes

Table 2: Sampling parameters for artificial parcel configurations. Each parcel attribute is sampled from a uniform distribution  $\mathcal{U}(a, b)$  with lower bound  $a$  and upper bound  $b$ .

parcel attribute	distribution
vorticity, $(\xi, \eta, \zeta)$	$\mathcal{U}(-10, 10)$
buoyancy, $b$	$\mathcal{U}(-1, 1)$
volume, $V$	$\mathcal{U}(V_{\min}/2, 3V_{\min}/2)$
aspect ratio, $\lambda_1 = a/c$	$\mathcal{U}(1, 4)$
aspect ratio, $\lambda_2 = a/b$	$\mathcal{U}(1, 4)$
azimuthal angle, $\theta$	$\mathcal{U}(0, 2\pi)$
polar angle, $\phi$	$\mathcal{U}(0, \pi)$

are uniformly sampled between  $[V_{\min}/2, 3V_{\min}/2]$  where  $V_{\min} = V_{\text{cell}}/40$  denotes the parcel volume threshold below which a parcel is considered small and therefore marked for merging. This test resulted in a total of 4,019,850,945 merge operations that were verified with the serial algorithm.

### 4.1 Example: Artificial parcel configuration

A parallel strong and weak scaling graph for 64 up to 65,536 cores is shown in Fig. 6. Note that we only use one AMD processor of a compute node when running with 64 cores. Each data point represents the total time averaged over 10 independent runs to complete 100 merge cycles, not including the cost of generating the artificial parcel configuration. Note that we always report the elapsed time of the slowest MPI rank. The standard deviation evaluated from the 10 runs is indicated by the error bars in the figure. All cycles start with a random sample of 20 parcels per grid cell where each parcel is assigned random properties as summarised in Table 2. The merge operation per cycle subsequently reduces the total number of parcels by about 36%. The strong scaling is performed for an isotropic grid of mesh spacing  $\Delta x = \Delta y = \Delta z = 5/16$  and  $1024^2 \times 32$  grid cells. In the case of the weak scaling, the grid starts with  $512^2 \times 32$  grid cells for 2 nodes and ends with  $8,192^2 \times 32$  grid cells for the 512-node run after we steadily increase the domain size to ensure an isotropic mesh spacing of 5/16. We choose a different number of horizontal and vertical grid points for these tests as this is representative of our target applications (atmospheric case studies), and the 2D domain decomposition we have pursued.

In Fig. 6, the total time (black line) includes the timings of parcel merging (red line), resolving graphs (green line) and building graphs (blue line). Up to 32 nodes, the timing is dominated by the graph construction (blue line), while for node-counts higher than 32, the graph resolution (green line) limits the scalability. The runtime of the graph resolution includes the execution time of the MPI RMA operations (purple line),



the calls to MPI barrier (orange line) and MPI allreduce (cyan line). The barrier synchronisation calls are

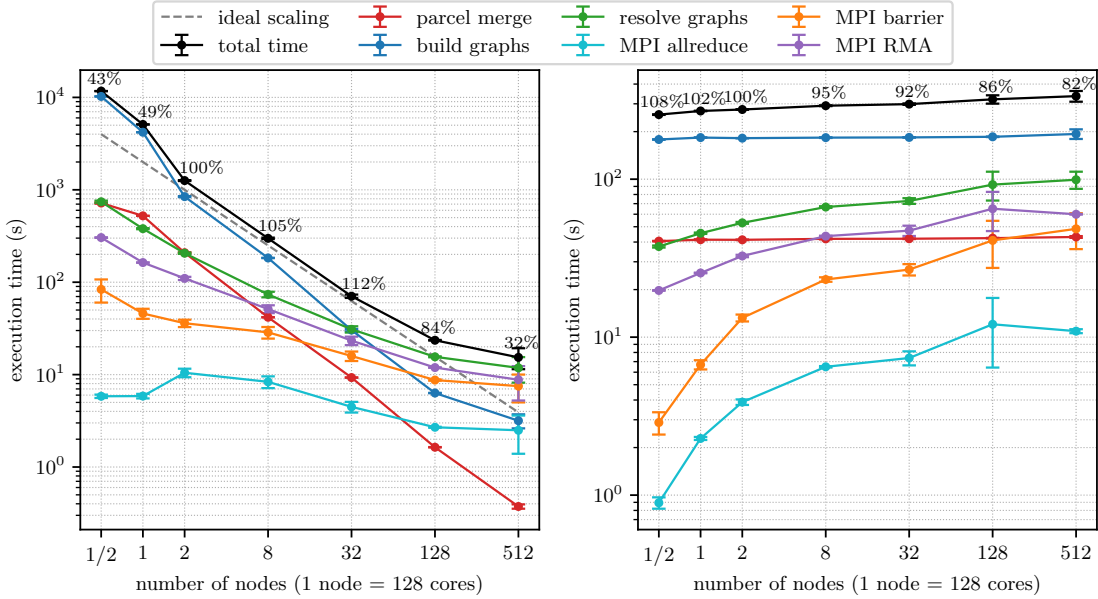


Figure 6: Parallel strong scaling (left panel) with  $1024^2 \times 32$  grid cells and parallel weak scaling (right panel) of the artificial parcel configuration example on 1/2 to 512 nodes on the ARCHER2 supercomputer. Each data point shows the maximum execution time across all MPI ranks averaged over 10 independent runs. The percentages on top of the black line denote the strong and weak parallel efficiencies. Note that the parallel efficiency is evaluated using the 2-node run as a baseline. The timing of the graph resolution (green line) includes all MPI related timers, i.e. MPI barrier (orange line), MPI RMA (purple line) and MPI allreduce (cyan line).

required at several stages of the graph resolution to prevent data race conditions due to concurrent RMA operations. The RMA operations denote the major cost during the graph resolution, followed by the barrier calls. Both MPI RMA and MPI barrier deteriorate the scalability for large MPI rank counts. The strong scaling efficiency decreases to 32% for 512 nodes. Note that we use the 2-node execution as the baseline for our efficiency calculations. In order to reduce this effect in flows with spatially localised active regions, our implementation uses a sub-communicator which only includes the MPI ranks that own at least one graph or share graph(s) with other MPI ranks across domain boundaries. This example resembles a globally active flow, therefore the sub-communicator is equivalent to the global MPI communicator. When running on a single node (128 cores), the strong scaling efficiency drops to 49%. On a single socket (64 cores) it amounts to 43%. We attribute this decline in performance to the ineffective use of the fast cache memory due to the increased memory usage per core and the poor data locality. In comparison, the same setup, but with half the number of grid cells in both horizontal directions, results in better performance for fewer than 2 compute nodes (cf. the left panel of Fig. 8). On the other hand, a doubling of the number of grid cells (right panel) leads to a performance drop like in Fig. 6 but for 2 compute nodes. The right panel of Fig. 6 shows the parallel scaling behaviour when the workload per core is kept constant with increasing number of cores (weak scaling). Overall, the weak scaling efficiency of the total time remains above 80% for this computationally balanced example. The strong and weak scaling efficiencies of the individual components of the algorithm are shown in Fig. 7. The parcel merging (red line) and graph construction (blue line) exhibit a superlinear speedup. We suspect this effect occurs mainly because of better cache usage, i.e. fewer cache misses and the reduction of the memory usage (Gustafson, 1990). In (Ristov et al., 2016) several other explanations for the phenomenon of superlinear speed-up are discussed. The actual process of merging parcels (red line) is a purely local operation. It is therefore expected to scale perfectly with increasing number of processes, as long as the workload is well-balanced between processes. However, since a parcel merge changes the position of parcel centres slightly, parcels close to subdomain boundaries may need to be communicated to other MPI

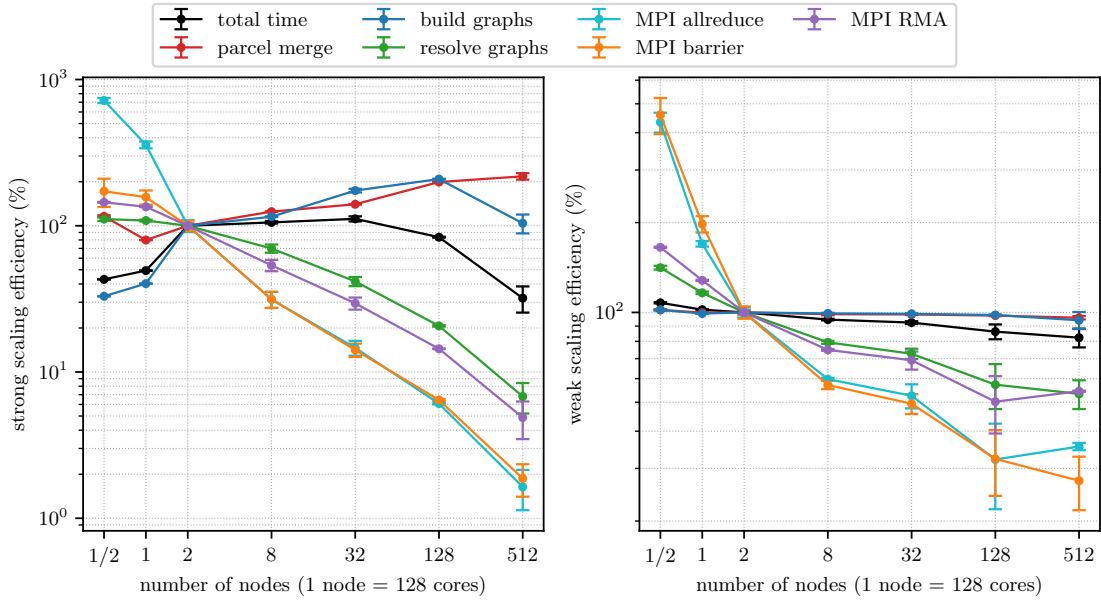


Figure 7: Strong (left panel) and weak (right panel) scaling efficiency corresponding to Fig. 6. The black line denotes the efficiency of the entire algorithm which consists of the parcel merging (red line), graph building (blue line) and graph resolution (green line). Note that the parallel efficiency is evaluated using the 2-node run as a baseline.

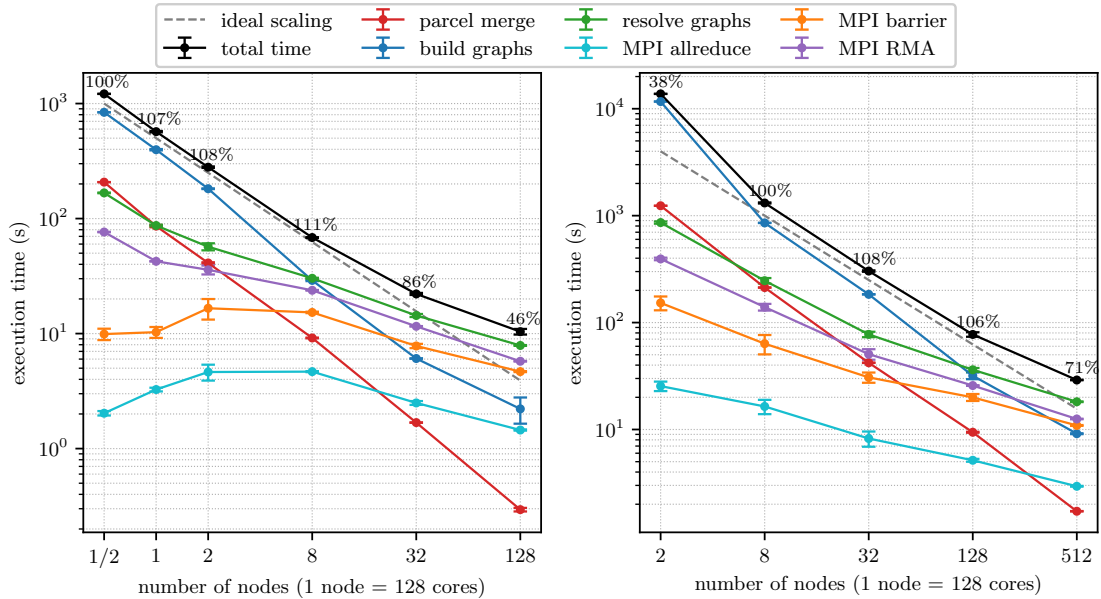


Figure 8: Strong scaling of the artificial parcel configuration example with  $512^2 \times 32$  grid cells (left panel) and  $2048^2 \times 32$  grid cells (right panel). Note that we use 8 nodes as the baseline for the efficiency calculation of the strong scaling on the right-hand side.

processes. That is why we must redistribute the parcels after every merge which involves eight neighbouring processes due to the two-dimensional Cartesian MPI domain decomposition. After the merge operation, a blocking MPI reduce is performed to obtain the new total number of parcels.

Up to the communication of parcel positions of small parcels in the MPI boundary regions and the global evaluation of any merging parcels, the construction of the graph structure is a local process, hence a nearly perfect scaling is expected as well. The main reasons for the reduction in performance are the RMA operations as well as the collective communication and synchronisation during the graph resolution step, which are clearly visible in the strong scaling efficiency in Fig. 7.

The minimum, maximum and average execution times over all MPI ranks for both strong ( $1024^2 \times 32$  grid cells) and weak scaling are gathered in Table 3 and Table 4, respectively. Again, the numbers are averaged over all 10 independent runs. Although the example is designed (statistically) to provide a balanced workload, the ratio between the slowest and fastest MPI ranks exceeds 2 for all MPI synchronisation and collective communication timers, which is highlighted by the red shaded cells. The same holds true for the MPI RMA operations when running with 8 or more nodes. Note that the MPI rank with the shortest MPI barrier timing is actually the slowest MPI rank because all other MPI ranks wait at the barrier for the slowest MPI rank to complete the call.

Table 3: Minimum (min), maximum (max) and average (avg) execution times in seconds over all MPI ranks for the strong scaling with  $1024^2 \times 32$  grid cells of the artificial parcel configuration example. The timings are averaged over 10 independent runs. Note that 1 compute node consists of 128 CPU cores. The cells coloured in red denote timings where the ratio between the slowest and fastest MPI ranks is above 2. The timing of the graph resolution (green line) includes all MPI related timers, i.e. MPI barrier (orange line), MPI RMA (purple line) and MPI allreduce (cyan line).

no. compute nodes		1/2	1	2	8	32	128	512
parcel merge	min	686.73	511.32	201.35	39.18	8.35	1.33	0.20
	avg	711.21	516.03	205.16	40.45	8.77	1.45	0.23
	max	719.03	522.49	208.56	41.74	9.29	1.64	0.37
build graphs	min	10 156.87	4157.57	826.37	176.98	27.67	6.05	2.73
	avg	10 206.33	4178.75	832.37	178.81	28.27	6.18	3.02
	max	10 242.41	4194.95	843.74	182.98	30.31	6.32	3.17
resolve graphs	min	656.68	340.98	188.61	67.96	28.22	15.32	11.64
	avg	693.29	357.71	199.61	71.72	30.24	15.43	11.73
	max	742.17	379.64	206.08	73.71	30.93	15.58	11.83
MPI allreduce	min	2.62	1.27	0.88	0.53	0.49	0.53	0.49
	avg	4.29	4.07	7.56	6.67	3.78	2.32	2.32
	max	5.83	5.86	10.48	8.35	4.48	2.69	2.50
MPI barrier	min	9.27	6.94	2.62	2.48	3.27	2.27	1.95
	avg	39.02	21.92	24.85	23.37	13.48	7.63	6.97
	max	83.65	45.86	35.99	28.64	15.90	8.73	7.51
MPI RMA	min	255.36	139.74	73.21	20.05	7.26	3.23	1.51
	avg	279.76	149.46	84.47	26.12	10.04	4.73	2.23
	max	304.03	163.16	110.01	51.26	23.31	11.92	8.80

## 4.2 Example: Rayleigh-Taylor instability

In this benchmark we test the nearest neighbour cluster algorithm based on a real physical application, the Rayleigh-Taylor instability (Rayleigh, 1882; Taylor, 1950), where we use exactly the same setup as in (Frey et al., 2023), but a grid resolution consisting of  $512^3$  grid cells. The flow is triggered by an unstably stratified buoyancy profile that features a horizontal perturbation which causes the flow to overturn. In

Table 4: Minimum (min), maximum (max) and average (avg) execution times in seconds over all MPI ranks for the weak scaling of the artificial parcel configuration example. The timings are averaged over 10 independent runs. Note that 1 compute node consists of 128 CPU cores. The cells coloured in red denote timings where the ratio between the slowest and fastest MPI ranks is above 2.

no. compute nodes		1/2	1	2	8	32	128	512
parcel merge	min	39.72	39.94	39.45	39.44	39.36	39.25	38.89
	avg	40.12	40.63	40.52	40.64	40.61	40.65	40.58
	max	40.53	41.39	41.32	41.90	41.97	42.34	43.06
build graphs	min	176.20	179.22	177.32	177.31	177.83	178.16	178.34
	avg	177.22	180.53	178.67	179.08	179.52	180.21	181.01
	max	178.31	183.40	181.84	183.25	183.85	185.46	193.23
resolve graphs	min	35.21	41.52	48.61	60.56	66.77	85.08	84.17
	avg	36.32	44.09	51.48	64.50	70.86	90.19	96.41
	max	37.46	45.48	52.91	66.62	72.79	92.37	99.19
MPI allreduce	min	0.22	0.23	0.38	0.55	0.81	0.80	1.31
	avg	0.56	1.56	2.76	5.03	5.80	10.22	9.01
	max	0.89	2.28	3.88	6.49	7.38	12.06	10.91
MPI barrier	min	1.17	1.17	1.68	2.86	4.20	5.27	11.08
	avg	2.09	4.82	9.86	18.40	21.68	35.24	42.09
	max	2.88	6.69	13.23	23.17	26.78	40.96	48.48
MPI RMA	min	17.27	20.53	19.84	20.05	21.03	21.38	21.58
	avg	18.47	22.29	23.63	25.43	26.82	27.82	28.21
	max	19.75	25.49	32.65	43.59	47.22	65.01	59.95

order to assess the parallel scalability we choose two stages of the flow that exhibit different workload distributions. At early times the flow is inhomogeneous with respect to the occurrence of very small parcels resulting in an imbalanced workload during the cluster algorithm, visible in the right panel of Fig. 9. The cluster algorithm is first invoked (the first parcels need merging) around time  $t \approx 2.76$  with 508 out of 4,096 MPI ranks corresponding to approximately 12.4%. At late times the flow is turbulent and the workload

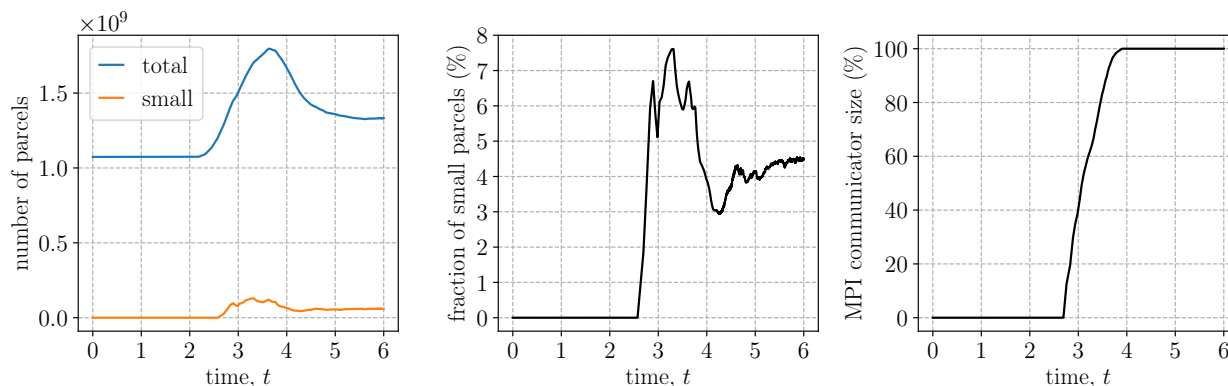


Figure 9: Evolution of the number of parcels (left panel), percentage of small parcels (centre panel) and the MPI sub-communicator size of the cluster algorithm (right panel). The first invocation of the cluster algorithm is around time  $t \approx 2.76$ . This data is generated using 4,096 CPU cores.

is homogeneously distributed. A cross-section with zoomed windows through the mid-plane  $y = 0$  with

the intersected ellipses at a late time, i.e.  $t = 6$ , is shown in Fig. 10. The total number of parcels in the

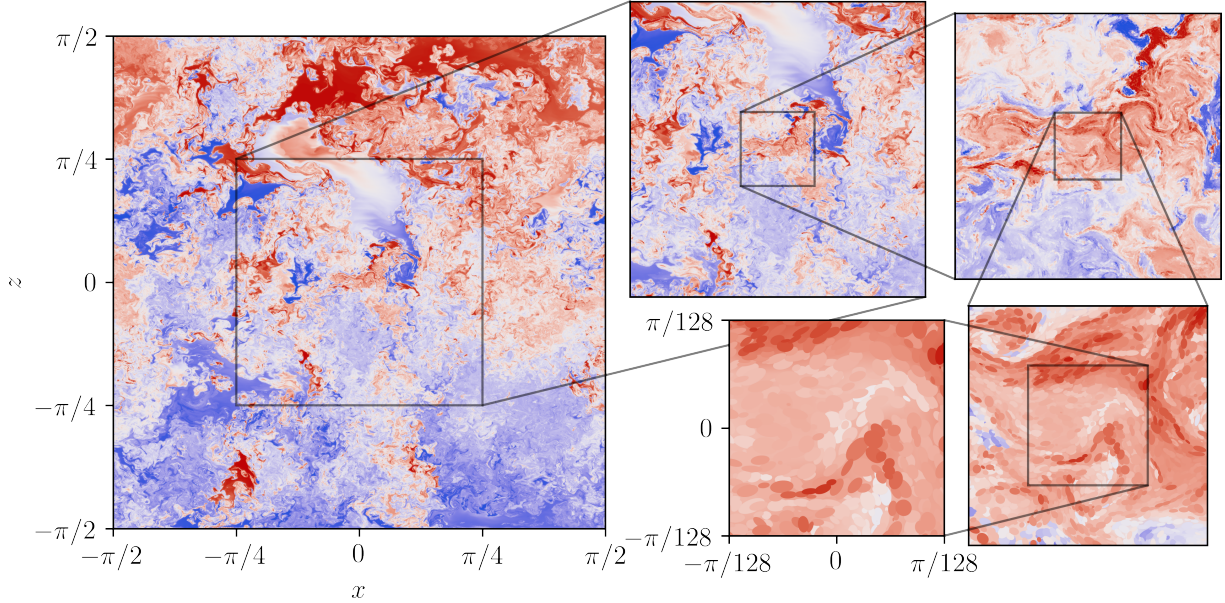


Figure 10: Cross sections with zoomed windows of the Rayleigh-Taylor instability at time  $t = 6$ . The cross sections also include the ellipses calculated by intersecting the three-dimensional ellipsoids with the  $xz$ -plane at  $y = 0$  (see in Frey et al. (2023) for a similar plot at a lower resolution).

simulation lies between  $10^9$  and  $2 \cdot 10^9$ , but the fraction of small parcels remains below 8% throughout the simulated time, as shown in the right and centre panel of Fig. 9. In Fig. 11 we report the cumulative sum of  $n$ -way mergers in the left panel and the total number of mergers in the right panel. As expected 2-way mergers represent the majority of clusters with about 98.7%, yet there are clusters involving up to 7 parcels. For both stages of the simulation, we generated ten parcel configurations of subsequent time steps starting at

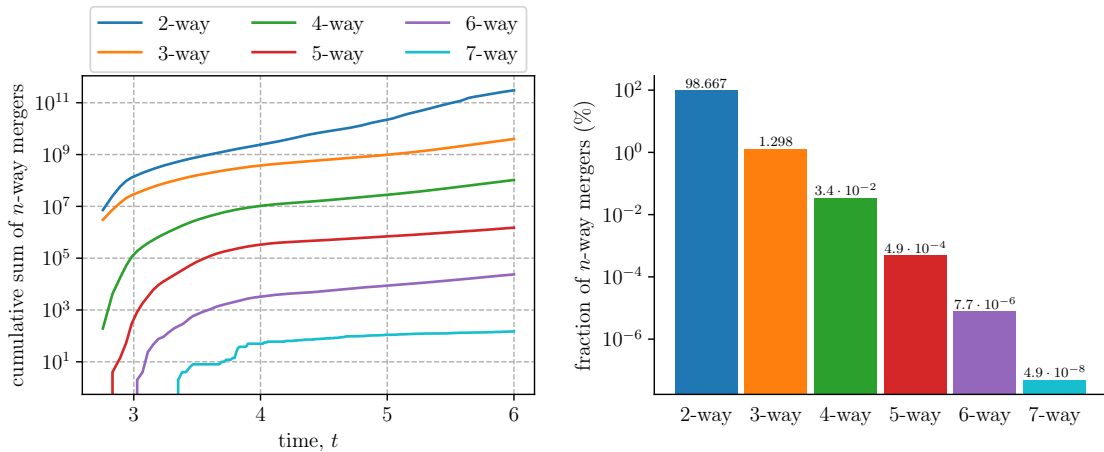


Figure 11: Cumulative sum of  $n$ -way cluster events (left panel) and percentage of total number of  $n$ -way cluster events (right panel) of the Rayleigh-Taylor instability test case up to time  $t = 6$ .

either  $t = 3$  or  $t = 6$ . In a bespoke benchmarking program we then iterate over the parcel configurations ten times and execute the cluster algorithm. The scaling result of the imbalanced setup for 256 to 16,384 cores

is shown in Fig. 12. Again, note that the reported timings are an average of the slowest MPI rank over 10

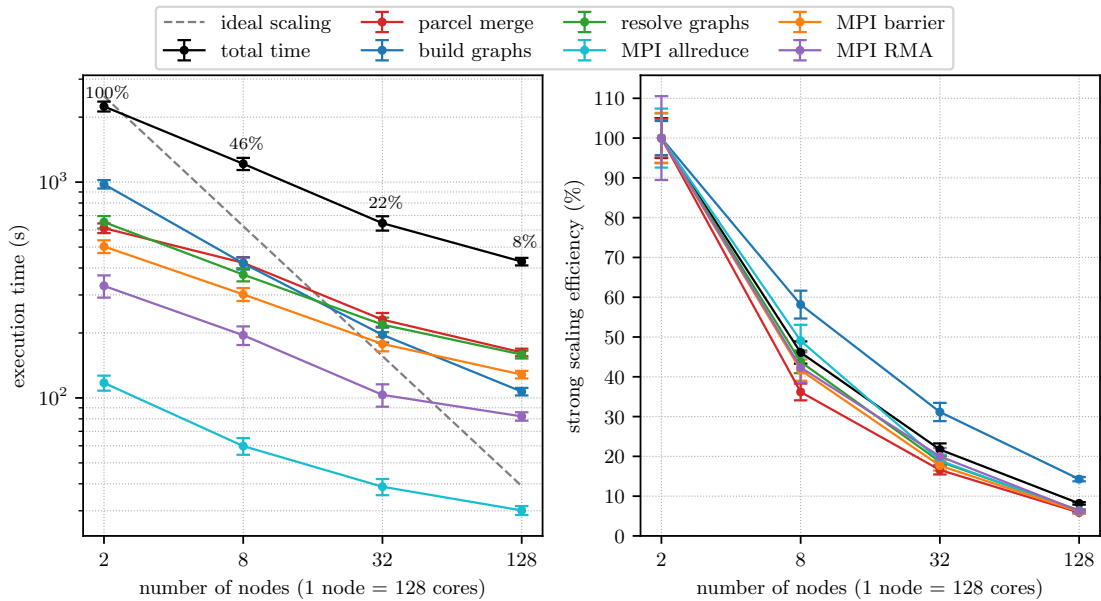


Figure 12: Parallel strong scaling (left panel) and strong scaling efficiency (right panel) at early times ( $t = 3$ ) for the Rayleigh-Taylor instability. Note that the timing of the graph resolution (green line) includes all MPI related timers, i.e. MPI barrier (orange line), MPI RMA (purple line) and MPI allreduce (cyan line).

independent runs. The left panel shows the speedup and the right panel the parallel strong scaling efficiency. The efficiency drastically decreases and is already below 70% for 1,024 cores. The dominating factor in the graph resolution (green line) step is the MPI barrier synchronisation (orange line). At late times where the workload is more homogeneously distributed, the cluster algorithm exhibits a much better parallel scalability with a parallel efficiency drop of 60% at 16,384 cores as shown in Fig. 13. Here, the MPI synchronisation calls (orange lines) and the MPI RMA operations (purple line) during the graph resolution step (green line) are the dominating factors. The variability of the timings among all MPI ranks for both cases is shown in Table 5 and Table 6. Note that the timings are evaluated with the global MPI communicator which is why the minimum time in the graph resolution (and timers contained therein) is zero for the imbalanced case where a sub-communicator is used for this part of the code.

In Table 7 we report the computational cost of the cluster algorithm in the context of the full  $N$ -body simulation (Frey et al., 2023) to run the Rayleigh-Taylor instability test case with  $512^3$  grid cells up to time  $t = 6$  (approximately 10,000 time steps) on 32 compute nodes. The table lists the timings of the parcel-to-grid `par2grid` and grid-to-parcel `grid2par` tri-linear interpolation, the vorticity inversion `vor2vel` and several parcel operations. The cluster algorithm contributes about 19% of the overall cost, where 17% are attributed to the MPI barrier synchronisation during the graph resolution. According to Fig. 9 we can consider the simulation to have an imbalanced workload in the cluster algorithm up to time 4. A strong scaling performing 75 time steps for time  $t > 6$  is shown in Fig. 14. In this regime, the computational costs are dominated by the interpolation routines (`par2grid` and `grid2par`), followed by the vorticity inversion `vor2vel`. Here, the cluster algorithm only contributes a minor fraction to the total costs.

Table 5: Minimum (min), maximum (max) and average (avg) execution times in seconds over all MPI ranks for the imbalanced strong scaling of the Rayleigh-Taylor instability. The timings are averaged over 10 independent runs. Note that 1 compute node consists of 128 CPU cores. The cells coloured in red denote timings where the ratio between the slowest and fastest MPI ranks is above 2.

no. compute nodes		2	8	32	128
parcel merge	min	84.12	16.79	0.70	0.10
	avg	126.74	80.52	47.03	26.63
	max	612.00	422.82	230.60	162.51
build graphs	min	122.73	22.61	4.56	1.99
	avg	497.48	149.98	40.35	13.27
	max	977.82	420.41	196.16	106.99
resolve graphs	min	0.00	0.00	0.00	0.00
	avg	459.60	217.80	129.41	97.64
	max	652.62	372.79	218.60	158.86
MPI allreduce	min	0.00	0.00	0.00	0.00
	avg	61.45	30.30	20.39	16.68
	max	117.43	59.84	38.77	30.11
MPI barrier	min	0.00	0.00	0.00	0.00
	avg	257.07	138.08	89.86	71.63
	max	503.28	301.92	177.94	128.32
MPI RMA	min	0.00	0.00	0.00	0.00
	avg	100.57	39.49	16.95	8.82
	max	330.58	195.19	103.34	82.12

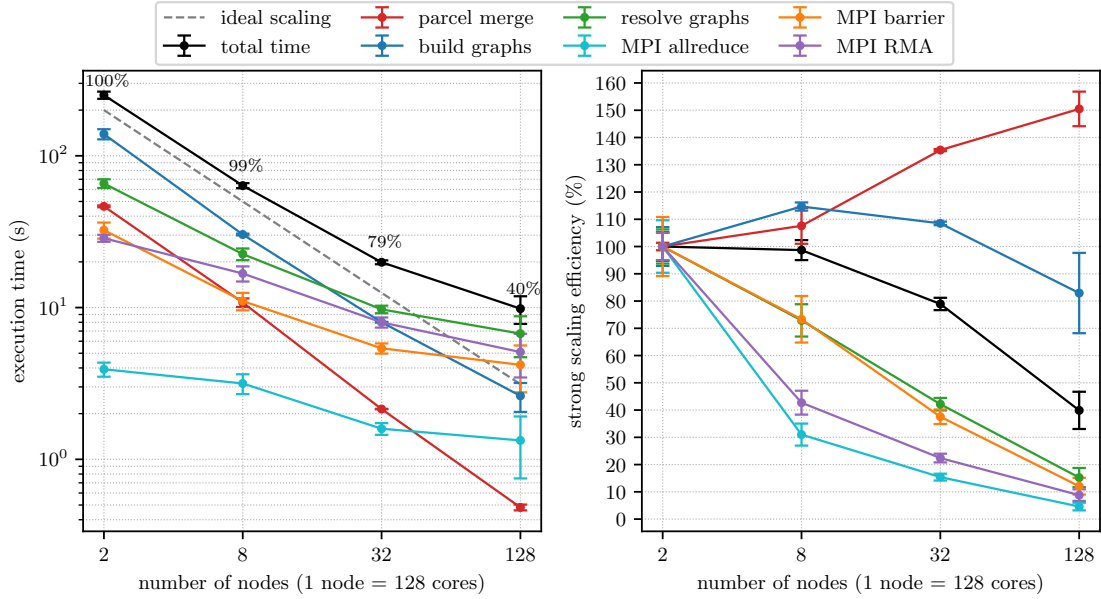


Figure 13: Parallel strong scaling (left panel) and strong scaling efficiency (right panel) at late times ( $t = 6$ ) for the Rayleigh-Taylor instability. Note that the timing of the graph resolution (green line) includes all MPI related timers, i.e. MPI barrier (orange line), MPI RMA (purple line) and MPI allreduce (cyan line).

Table 6: Minimum (min), maximum (max) and average (avg) execution times in seconds over all MPI ranks for the balanced strong scaling of the Rayleigh-Taylor instability. The timings are averaged over 10 independent runs. Note that 1 compute node consists of 128 CPU cores. The cells coloured in red denote timings where the ratio between the slowest and fastest MPI ranks is above 2.

no. compute nodes		2	8	32	128
parcel merge	min	41.02	9.65	1.79	0.35
	avg	44.02	9.98	1.90	0.39
	max	46.44	10.79	2.14	0.48
build graphs	min	126.64	28.94	7.62	2.48
	avg	132.41	29.57	7.77	2.53
	max	138.98	30.30	8.01	2.62
resolve graphs	min	53.73	21.24	9.35	6.57
	avg	60.09	21.84	9.52	6.65
	max	65.64	22.51	9.73	6.73
MPI allreduce	min	0.69	0.28	0.17	0.27
	avg	2.83	2.49	1.34	1.18
	max	3.92	3.16	1.59	1.33
MPI barrier	min	12.83	2.07	0.96	1.09
	avg	24.48	8.94	4.56	3.74
	max	32.38	11.04	5.39	4.20
MPI RMA	min	15.49	5.10	2.15	1.02
	avg	19.74	7.67	3.20	1.62
	max	28.63	16.76	7.99	5.09



Table 7: Minimum (min), maximum (max) and average (avg) execution times in seconds over all MPI ranks for the full  $N$ -body simulation. Note that we only report the timings of components that are common to most  $N$ -body simulation models. This the Rayleigh-Taylor instability simulation is performed on 32 compute nodes (4,096 CPU cores).

model component	no. calls	percentage of time (%)	min time (s)	avg time (s)	max time (s)
total	1	100.00	98 895	98 895	98 895
vor2vel	50 071	25.58	8955	25 296	26 444
par2grid	50 071	14.65	13 536	14 489	31 047
grid2par	50 071	20.40	19 280	20 177	21 418
parcel split	10 014	1.66	1587	1641	1861
parcel merge	10 014	0.21	173	205	296
parcel push	10 014	4.59	3243	4543	21 549
build graphs	10 014	1.21	1004	1192	17 628
resolve graphs	9997	17.71	1026	17 512	17 617
MPI allreduce	50 637	0.17	46	168	202
MPI barrier	171 905	17.18	167	16 994	17 194

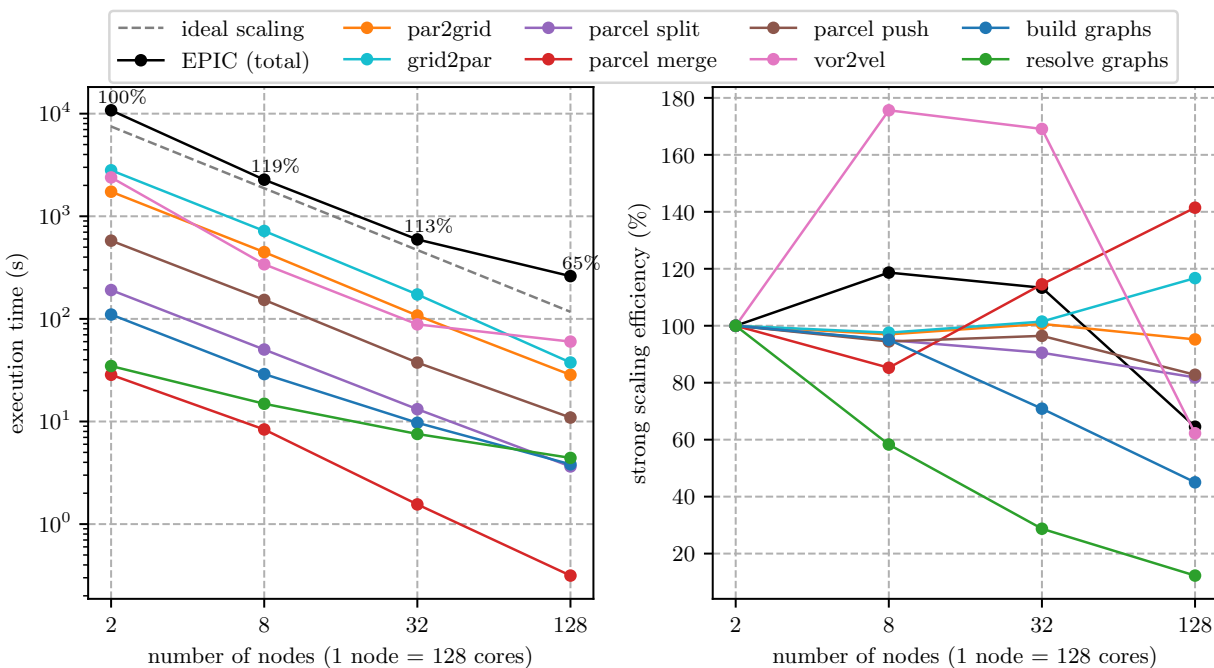


Figure 14: Parallel strong scaling (left panel) and parallel strong scaling efficiency (right panel) when running 75 time steps of the full  $N$ -body Rayleigh-Taylor instability simulation in the balanced workload regime ( $t \geq 6$ ).

## 5 Conclusions

We have presented the parallel performance of a clustering algorithm based on a nearest neighbour search using the Euclidean distance as a metric for proximity. The algorithm is used for the merging of objects (here: parcels of ellipsoidal shape) in  $N$ -body simulations. The graph structures are simplified in an iterative procedure which makes use of one-sided MPI communication with passive target synchronisation. We assessed the parallel performance based on artificial  $N$ -body configurations as well as configurations extracted from a Rayleigh-Taylor fluid flow instability simulation. The artificial example demonstrates the parallel performance for a balanced workload scenario. Here, the parallel algorithm shows good strong and weak parallel scalability up to 65,536 CPU cores for grids ranging from  $512^2 \times 32$  to  $8192^2 \times 32$  grid cells. The overall parallel weak scaling efficiency does not drop below 80%. On the other hand, the parallel performance using parcel configurations generated from a Rayleigh-Taylor instability simulation with  $512^3$  grid cells shows a different scaling result dependent on the workload distribution. At early times ( $t \approx 3$ ) the number of merge events is inhomogeneously distributed and thus results in an imbalanced workload. The parallel efficiency therefore quickly falls to 8% when the computing power is increased to 16,384 CPU cores, which corresponds to an increase in computing power by a factor 64. At late times ( $t > 6$ ), the flow exhibits homogeneous isotropic turbulence, thereby distributing the computational load more evenly. In this regime, the parallel efficiency with 16,384 CPU cores drops to around 40% compared to processing with 256 CPU cores. A detailed performance analysis has shown that the parallel scalability is limited by the collective communication and synchronisation calls, as well as the RMA operations during the graph resolution step. In future work, we therefore aim to improve the performance through algorithmic changes that allow us to reduce the number of collective MPI calls (i.e. synchronisation barriers and global reductions) that affect parallel scalability.

### Code availability

The source code of the EPIC method and the testing codes for the benchmarks are publicly available. The testing codes are shipped with the EPIC source code and found in the directory `mpi-tests`. This paper uses EPIC version 0.14.2 (Frey et al., 2024).

### Acknowledgements

We thank David Dritschel for his valuable feedback on the manuscript prior to submission. This work used the ARCHER2 UK National Supercomputing Service (<https://www.archer2.ac.uk>) which is funded and managed by UKRI and supported by EPCC, HPE and The University of Edinburgh.

### Funding

The author(s) disclosed receipt of the following financial support for the research, authorship, and/or publication of this article: This work was supported by the UK Engineering and Physical Sciences Research Council [grant numbers EP/T025301/1, EP/T025409/1].

## References

- Bentley JL (1975) A survey of techniques for fixed radius near neighbor searching. Technical report, Stanford, CA, USA.
- Bentley JL, Stanat DF and Williams E (1977) The complexity of finding fixed-radius near neighbors. *Information Processing Letters* 6(6): 209–212. DOI:10.1016/0020-0190(77)90070-9.
- Domínguez JM, Crespo AJC, Gómez-Gesteira M and Marongiu JC (2011) Neighbour lists in smoothed particle hydrodynamics. *International Journal for Numerical Methods in Fluids* 67(12): 2026–2042. DOI: 10.1002/flid.2481.
- Eppstein D, Paterson MS and Yao FF (1997) On nearest-neighbor graphs. *Discrete & Computational Geometry* 17(3): 263–282. DOI:10.1007/PL00009293.

- Frey M, Böing S, Dritschel D and Apóstolo R (2024) EPIC-model/epic: EPIC version 0.14.2. DOI:10.5281/zenodo.13120965.
- Frey M, Dritschel D and Böing S (2022) EPIC: The Elliptical Parcel-In-Cell method. *Journal of Computational Physics: X* 14: 100109. DOI:10.1016/j.jcpx.2022.100109.
- Frey M, Dritschel D and Böing S (2023) The 3D Elliptical Parcel-In-Cell (EPIC) method. *Journal of Computational Physics: X* 17: 100136. DOI:10.1016/j.jcpx.2023.100136.
- Ghosh S, Halappanavar M, Kalyanaraman A, Khan A and Gebremedhin AH (2019) Exploring mpi communication models for graph applications using graph matching as a case study. In: *2019 IEEE International Parallel and Distributed Processing Symposium (IPDPS)*. pp. 761–770. DOI:10.1109/IPDPS.2019.00085.
- Ghosh S, Hammond JR, Peña AJ, Balaji P, Gebremedhin AH and Chapman B (2016) One-sided interface for matrix operations using mpi-3 rma: A case study with elemental. In: *2016 45th International Conference on Parallel Processing (ICPP)*. pp. 185–194. DOI:10.1109/ICPP.2016.28.
- Gustafson J (1990) Fixed time, tiered memory, and superlinear speedup. In: *Proceedings of the Fifth Distributed Memory Computing Conference, 1990.*, volume 2. pp. 1255–1260. DOI:10.1109/DMCC.1990.556383.
- Hoefler T, Dinan J, Thakur R, Barrett B, Balaji P, Gropp W and Underwood K (2015) Remote memory access programming in MPI-3. *ACM Trans. Parallel Comput.* 2(2). DOI:10.1145/2780584.
- Jiang W, Liu J, Jin HW, Panda D, Gropp W and Thakur R (2004) High performance mpi-2 one-sided communication over infiniband. In: *IEEE International Symposium on Cluster Computing and the Grid, 2004. CCGrid 2004*. pp. 531–538. DOI:10.1109/CCGrid.2004.1336648.
- Message Passing Interface Forum (1997) *MPI-2: Extensions to the Message-Passing Interface*. URL <https://www.mpi-forum.org/docs/mpi-2.0/mpi-20.ps>.
- Message Passing Interface Forum (2012) *MPI: A Message-Passing Interface Standard Version 3.0*. URL <https://www.mpi-forum.org/docs/mpi-3.0/mpi30-report.pdf>.
- Quentrec B and Brot C (1973) New method for searching for neighbors in molecular dynamics computations. *Journal of Computational Physics* 13(3): 430–432. DOI:10.1016/0021-9991(73)90046-6.
- Rayleigh (1882) Investigation of the Character of the Equilibrium of an Incompressible Heavy Fluid of Variable Density. *Proceedings of the London Mathematical Society* s1-14(1): 170–177. DOI:10.1112/plms/s1-14.1.170.
- Ristov S, Prodan R, Gusev M and Skala K (2016) Superlinear speedup in hpc systems: Why and when? In: *2016 Federated Conference on Computer Science and Information Systems (FedCSIS)*. pp. 889–898. DOI:10.15439/2016F498.
- Sawyer WB and Mirin AA (2007) The implementation of the finite-volume dynamical core in the community atmosphere model. *Journal of Computational and Applied Mathematics* 203(2): 387–396. DOI:10.1016/j.cam.2006.04.015.
- Schuchart J, Niethammer C, Gracia J and Bosilca G (2021) Quo Vadis MPI RMA? Towards a More Efficient Use of MPI One-Sided Communication. *arXiv e-prints* DOI:10.48550/arXiv.2111.08142.
- Taylor GI (1950) The instability of liquid surfaces when accelerated in a direction perpendicular to their planes. I. *Proceedings of the Royal Society of London. Series A. Mathematical and Physical Sciences* 201(1065): 192–196. DOI:10.1098/rspa.1950.0052.
- Verlet L (1967) Computer "Experiments" on Classical Fluids. I. Thermodynamical Properties of Lennard-Jones Molecules. *Phys. Rev.* 159: 98–103. DOI:10.1103/PhysRev.159.98.

- Yamazaki I, Chow E, Bouteiller A and Dongarra J (2019) Performance of asynchronous optimized Schwarz with one-sided communication. *Parallel Computing* 86: 66–81. DOI:10.1016/j.parco.2019.05.004.
- Yuval G (1975) Finding near neighbours in k-dimensional space. *Information Processing Letters* 3(4): 113–114. DOI:10.1016/0020-0190(75)90044-7.
- Yuval G (1976) Finding nearest neighbours. *Information Processing Letters* 5(3): 63–65. DOI:10.1016/0020-0190(76)90064-8.
- Zhao X, Balaji P and Gropp W (2016) Scalability challenges in current MPI one-sided implementations. In: *2016 15th International Symposium on Parallel and Distributed Computing (ISPDC)*. pp. 38–47. DOI: 10.1109/ISPDC.2016.14.